Earthline Journal of Chemical Sciences
E-ISSN: 2581-9003; CODEN: EJCSB4
Volume 12, Number 3, 2025, Pages 343-357
https://doi.org/10.34198/ejcs.12325.343357

Removal of zinc from water using graphene-like biochar produced from palm seed shells

Yacouba Zoungranan*

Département de Mathématiques Physique Chimie (MPC), Université Peleforo GON COULIBALY,
B.P. 1328 Korhogo, Côte d'Ivoire
e-mail: zoungranan@gmail.com

Djè Daniel Yannick

Laboratoire de Thermodynamique et de Physico-Chimie du Milieu (LTPCM), Université NANGUI ABROGOUA,
02 BP 802 Abidjan 02, Côte d'Ivoire

Assouma Dagri Cyrille

Département de Mathématiques Physique Chimie (MPC), Université Peleforo GON COULIBALY,
B.P. 1328 Korhogo, Côte d'Ivoire

Ouattara Daouda

Laboratoire de Thermodynamique et de Physico-Chimie du Milieu (LTPCM), Université NANGUI ABROGOUA,
02 BP 802 Abidjan 02, Côte d'Ivoire

Ekou Lynda

Laboratoire de Thermodynamique et de Physico-Chimie du Milieu (LTPCM), Université NANGUI ABROGOUA,
02 BP 802 Abidjan 02, Côte d'Ivoire

Abstract

Water pollution by trace metals poses a serious threat to both human health and the environment, making their removal from contaminated water a critical issue. Recent research has focused on identifying efficient and sustainable adsorbents. In this study, oil palm seed shells (*Elaeis guineensis*) were used to synthesize graphene-like biochar (BGp), which was then partially oxidized to obtain oxidized biochar (BOGp), aimed at removing zinc from aqueous solutions via adsorption. Characterization of the materials revealed low moisture content and high ash content for both BGp and BOGp. Their bulk densities were 0.76 g/cm³ (BGp) and 0.71 g/cm³ (BOGp), while the point of zero charge (pH_pzc) values were 7.3 and 4, respectively. X-ray diffraction (XRD) analysis showed distinct peaks at $2\theta \approx 10°$ and $2\theta \approx 26.03°$, characteristic of oxidized graphitic carbon. BOGp exhibited a higher BET specific surface area (340.32 m²/g) compared to BGp (228.20 m²/g). Infrared (FTIR) spectroscopy confirmed the oxidation of BOGp through intensified C=O stretching vibrations. Both materials demonstrated high zinc removal efficiencies. Using 0.1 g of adsorbent in 50 mL of a 1 mg/L zinc sulfate solution, removal rates of 73.4% (BGp) and 90.11% (BOGp) were achieved. The adsorption processes followed pseudo-second-order kinetics and were characterized as chemisorption. The Freundlich and Temkin isotherm models, indicating multilayer and exothermic adsorption, confirmed the effectiveness of both materials. This study underscores a sustainable and value-added approach to utilizing agricultural waste for water treatment applications.

Received: July 14, 2025; Accepted: August 11, 2025; Published: August 14, 2025

Keywords and phrases: graphene-like biochar, adsorption, oxidation, zinc.

*Corresponding author

1. Introduction

The contamination of water resources by trace metals (TMs) represents a significant environmental concern, attracting increasing attention from the scientific community and environmental regulatory agencies. Mining and industrial processes, particularly alloy production, substantially contribute to the accumulation of these metals in aquatic ecosystems [1] . Among them, zinc is particularly noteworthy: although it is an essential micronutrient at low concentrations, it becomes toxic at elevated levels. The World Health Organization (WHO) has established a maximum permissible concentration of 5 mg/L for zinc in drinking water, underscoring the need for stringent environmental control of its presence [2]. Zinc can disrupt the metabolism of aquatic organisms, especially by impairing reproductive functions [3]. Conventional wastewater treatment methods include chemical precipitation, ion exchange, filtration, solvent extraction, and adsorption. However, several of these techniques suffer from significant drawbacks, such as sludge generation in precipitation processes or the high operational costs associated with membrane filtration and electrodialysis [4]. Within this context, adsorption has emerged as a promising, sustainable, and cost-effective method for heavy metal removal, particularly when using low-cost, natural adsorbents like biochar [5]. Graphene-like biochar, derived from carbon-rich biomass and employed as a graphene precursor, exhibits remarkable adsorption capacity owing to its high specific surface area and advantageous microporous structure [6]. Prior studies have confirmed its effectiveness in capturing a wide range of contaminants [7,8]. This research project aims to investigate the synthesis and characterization of graphene-like biochar and oxidized graphene, with a focus on their adsorption efficiency for zinc. The study will explore the underlying mechanisms and assess the influence of key experimental variables, thereby enhancing our understanding of metal–adsorbent interactions. The findings could offer valuable insights for the development of more efficient and sustainable wastewater treatment technologies.

2. Materials and Methods

2.1. Graphene-like biochar adsorbents

The synthesis of graphene-like biochar (BGp) was carried out in three steps following the method of Xiao [9], with some modifications. The graphitization-activation step involved producing graphitized biochar through hot impregnation of the dry shells with iron chloride ($FeCl_3$), followed by activation of the graphitized biochar using zinc chloride ($ZnCl_2$). The oxidation of BGp to BOGp was performed according to the procedure described by Panicker [10], with a few modifications. All modifications have been detailed in our previous studies [11,12].

2.2. Physicochemical properties and characterization tests

2.2.1. Chemical properties

Moisture content: A sample of the adsorbent is placed in a ceramic crucible of known mass (m_1). The total mass of the crucible and biochar is denoted as m_2. After drying in an oven at 105 °C for 24 hours, the mass of the assembly is recorded as m_3. The humidity rate (H) is then determined using the following formula:

$$H\,(\%) = \frac{m_3 - m_1}{m_2 - m_1} \times 100 \tag{1}$$

Ash content: The determination of the inorganic fraction of the adsorbent follows the same protocol as the humidity measurement. A sample of the adsorbent is placed in a ceramic crucible of known initial mass (m_1). The total mass of the crucible and biochar is then recorded as m_2. After drying in an oven at 105 °C for 24 hours, the sample is calcined at 650 °C for one hour. Once cooled, the mass of the assembly is recorded as m_4.

$$Ash\,(\%) = \frac{m_4 - m_1}{m_2 - m_1} \times 100 \tag{2}$$

Density: An empty 100 mL graduated cylinder is weighed, and its initial mass is recorded as M_0. The cylinder is then filled to the calibration mark with the adsorbent. The entire setup is weighed again, and the new mass is recorded as M_1.

$$d = \frac{M_1 - M_0}{100} \tag{3}$$

pH at the point of zero charge (pH_{pzc}): The pH at the point of zero charge (pH_{pzc}) is defined as the pH at which the total net surface charge of the adsorbent is zero, despite the presence of localized positive and negative charges [13]. Five 0.1 mol/L NaCl solutions with initial pH values ranging from 2 to 14 (adjusted using NaOH or HCl and measured with a HANNA HI 98 pH meter) were prepared. Each solution was mixed with 0.1 g of adsorbent and agitated for 48 hours. After filtration, the final pH_f was measured. The pH_{pzc} was determined as the intersection point of the $pH_f = f(pH_i)$ curve with the $pH_f = pH_i$ line.

Iodine number: The iodine number is a key indicator used to evaluate the adsorption capacity of an adsorbent's micropores, providing an estimate of its micropore volume. The test involved placing a mass m = 0.05 g of the adsorbent in contact with 20 mL of a 0.1 N iodine solution for 5 minutes. After filtration, 10 mL of the filtrate were titrated with a 0.1 N sodium thiosulfate solution, using starch paste as an indicator. A blank test was also performed under the same conditions, without the adsorbent. The iodine number (Id), expressed in mg/g, was then calculated using the following equation:

$$Id = \frac{V_0 - V}{m} \times 12.69 \tag{4}$$

V_0: Volume (mL) of thiosulfate at equivalence for the blank test,

V: Volume (mL) of thiosulfate at equivalence for the sample with the adsorbent.

2.2.2. Structural and morphological analysis

The structural phases of BGp and BOGp were determined by X-ray diffraction using a GBC-EMMA diffractometer (Braeside, Victoria, Australia) equipped with CuKα radiation (λ = 0.154 nm). The samples were analyzed over 2θ range of 0.15° to 91° with a step size of 0.02°.

The morphology of BGp and BOGp was examined using a field-emission scanning electron microscope (Zeiss SIGMA 300Graz, Austria).

2.2.3. Surface characterization

Fourier transform infrared (FTIR) spectroscopy was used to identify the functional groups present in the adsorbent material. The analysis was performed using a FTIR spectrometer (Nicolet 6700 Thermo Scientific), with potassium bromide (KBr) pellets as the sample medium.

The specific surface area, pore volume, and average pore diameter of BGp and BOGp were determined by nitrogen physisorption using the Brunauer-Emmett-Teller (BET) method. These measurements were conducted using a surface area and porosity analyzer (Micromeritics TriStar II 3020, Georgia, USA).

2.2.4. Thermogravimetric analysis

Thermogravimetric analysis (TGA) was performed using a Setsys Evolution 16 analyzer (Setaram, Panteleimon, Romania) under controlled conditions.

2.3. Batch adsorption study

2.3.1. Methodology

For all experiments, a stock solution of zinc sulfate with a concentration of C = 50 mg/L was carefully prepared. Different test concentrations (C_i) were obtained by diluting this stock solution. For each test, a mass of m = 0.1 g of each adsorbent was placed in a 250 mL flask containing V_i = 50 mL of zinc sulfate solution at concentration C_i. The zinc-adsorbent mixture was then agitated at 300 rpm using an orbital shaker (HeidolphVibramax 100, Germany) for a specified time (t). After agitation, the mixture was filtered to obtain a final volume (V_f). The residual zinc concentration (C_f) was measured using an atomic absorption spectrometer (Thermo Scientific iCE 3000, AA05162102 v1.30) at a wavelength of 213.9 nm. Both initial (C_i) and final (C_f) concentrations were determined using a calibration curve generated from zinc sulfate solutions in distilled water. The adsorption capacity (q) of BGp or BOGp was calculated using the following equation:

$$q = \frac{C_i V_i - C_f V_f}{m} \tag{5}$$

The zinc removal efficiency (%) at any given contact time is calculated using the following equation:

$$E(\%) = \frac{C_0 - C_t}{C_0} \times 100 \tag{1}$$

where C_0 (mg/L) represents the initial zinc concentration in the solution, and C_t (mg/L)is the zinc concentration at time t.

2.3.2. Physicochemical parameter effects

Contact time: The adsorption reaction kinetics were investigated by placing 0.1 g of adsorbent in each of eight beakers containing 50 mL of zinc solution at an initial concentration of $C_i = C_0$ = 1 mg/L. For each beaker, eight agitation times were tested: 5, 10, 15, 30, 45, 60, 90, and 120 minutes.

Initial Zinc Concentration: The influence of the initial zinc concentration on adsorption efficiency was evaluated using concentrations of 1, 2, 4, 6, 8, and 10 mg/L. For these tests, the agitation time (t) was fixed at 1 hour under 300 rpm stirring.

Adsorbent mass: The impact of adsorbent mass was examined by testing different quantities (0.1, 0.2, 0.3, 0.4, and 0.5 g) in a zinc sulfate solution ($C_i = C_0$ = 1 mg/L) under 300 rpm agitation for 1 hour.

2.3.3. Postulated adsorption kinetic and isotherm models

To complete the adsorption kinetics study, pseudo first order second order, Elovich and intra-particle diffusion kinetic models were applied to experimental data. The key characteristics of these models are summarized in Table 1.

Table 1. Kineticmodels

Model	Equation	Parameters
Pseudo first order	$\log(q_e - q_t) = \log(q_e) - \frac{k_1}{2.303}t$ (7)	- k_1 (min^{-1}): Pseudo-first order rate constant - q_e (mg g^{-1}): Theoretical equilibrium adsorption capacity
Pseudo second order	$\frac{t}{q_t} = \frac{1}{k_2 q_e^2} + \frac{1}{q_e}t$ (8)	- k_2 ($g \cdot mg^{-1} \cdot min^{-1}$): Rate constant of pseudo-second order - q_e (mg g^{-1}): Theoretical equilibrium adsorption capacity
Elovich	$q = \frac{1}{\beta}\ln(\alpha\beta) + \frac{1}{\beta}\ln t$ (9)	- α is the initial adsorption rate ($mg \cdot g^{-1} \cdot min^{-1}$) - β is the desorption constant related to the surface area
Intra-particle diffusion	$q_t = K_d\sqrt{t} + C$ (10)	- Kd ($mg/g.min^{0.5}$) is a diffusion constant - C is the boundary layer thickness

The equilibrium adsorption behavior was evaluated using the Langmuir, Freundlich, and Temkin isotherm models, which describe the relationship between the equilibrium concentration of zinc (Ce) and the amount adsorbed (qe) on the surface of each adsorbent. The mathematical expressions of these models are presented in Table 2.

Table 2. Adsorption isotherm models

Model	Equation	Parameters
Langmuir	$\frac{C_e}{q_e} = \frac{1}{q_m K_L} + \frac{1}{q_m}C_e$ (11)	- K_L ($L.mg^{-1}$) : Langmuir constant - q_m (mg g^{-1}): Maximum zinc adsorption capacity
Freundlich	$\log(q_e) = \log K_F + \frac{1}{n}\log C_e$ (12)	- K_F($L.mg^{-1}$): Freundlich constant - 1/n (dimensionless): heterogeneity factor)
Temkin	$q_e = \frac{RT}{b_T}\ln K_T + (\frac{RT}{b_T})\ln C_e$ (13)	- K_T ($L.g^{-1}$): Temkin coefficient related to binding energy - b_T ($J.mol^{-1}$): This coefficient reflects the average adsorption energy

2.4. Raw data processing

All calculations and graphical representations were carried out using Microsoft Office Excel 2016 Professional and OriginPro 2018. The mean values and standard deviations were calculated based on three independent measurements.

3. Results and Discussion

3.1. Chemical properties of the adsorbents

The results of the chemical property analysis of the adsorbents are summarized in Table 3.

Table 3. Some chemical properties of the adsorbents used in the study

	BGp	**BOGp**
Moisture content (%)	9,51	7,62
Ash content (%)	11,74	11,25
Density (g/cm^3)	0,76	0,71
Iodine numer (mg/g)	389,21	228,42
pH*pzc*	7,3	4

The adsorbents BGp and BOGp exhibit high ash contents, although remaining below 15%. These elevated ash levels are attributed to the metallic enrichment that occurred during the graphitization-activation process, which involved the use of metal chlorides. However, both materials display relatively low moisture contents, below 10%, indicating their potential efficiency for adsorption processes. Low moisture content suggests that fewer adsorption sites are occupied by water, leaving more available sites for other species such as zinc ions.

Both BGp and BOGp also show high densities, though less than 1 g/cm³, which implies that the adsorbents can remain suspended in solution and benefit from good solvation, enhancing mass transfer in the liquid phase.

Iodine number results indicate that BGp possesses a more developed microporosity than BOGp. The iodine number of BGp exceeds the 352 mg/g reported by Anderson et al. [14] for standard biochar yet remains significantly lower than the 979 mg/g observed for activated carbon by the same authors. These findings suggest that the microporosity of both BGp and BOGp is not fully developed and that their adsorption mechanisms may be influenced by other physicochemical.

Regarding the pHpzc (point of zero charge), surface charges are positive at pH values below this point. Specifically, surface charges are positive for pH values below 7.3 for BGp and below 4 for BOGp. At pH values above the pHpzc, the surface charges become negative.

3.2. Characterizations

3.2.1. Structure and morphology

The X-ray diffraction peak intensities (Figure 1) observed for both materials indicate a high degree of graphitization, approaching a structure like that of grapheme [15]. Notably, when transitioning from BGp to BOGp, a greater number of peaks appears, while their intensities decrease. This phenomenon may be attributed to the double oxidation undergone by BGp. Moreover, the X-ray diffraction (XRD) patterns of BGp and BOGp reveal a distinct peak at $2\theta \approx 26.03°$, typical of graphitic carbon [15]. Additional peaks are observed at $2\theta \approx 10°$ and $2\theta \approx 43°$ in the BOGp diffractogram, which are characteristic of oxidized graphitic carbon [15]. The results of SEM (Scanning Electron Microscopy) analysis (Figure 2) show that BGp exhibits a heterogeneous surface at the nanoscale. The presence of cavities, pores, and brighter regions corresponding to crystallized (and thus denser) zones is observed [16].

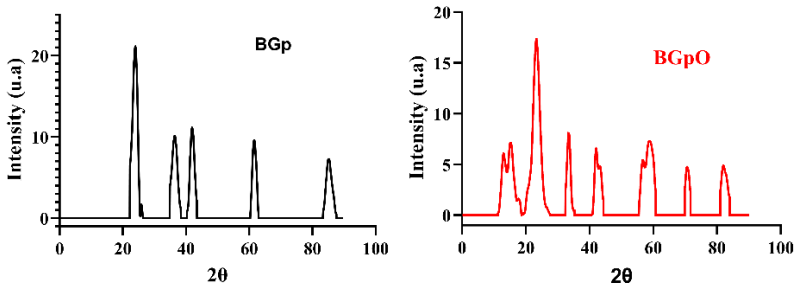

Figure 1. XRD patterns of the adsorbents.

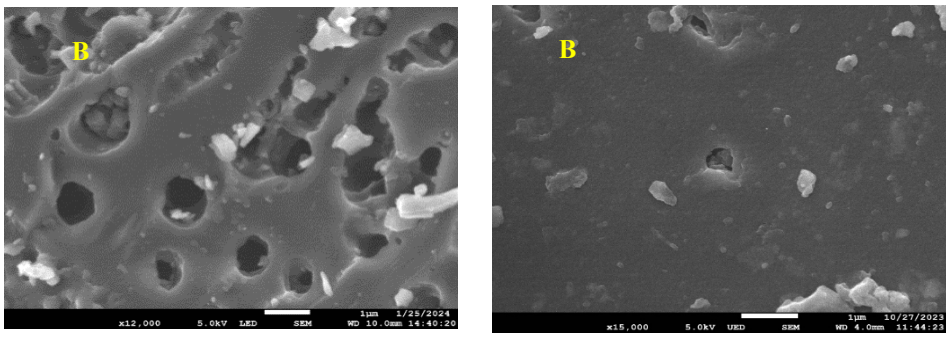

Figure 2. SEM images of the adsorbents.

The lamellar structure of the material, characteristic of graphene, may have contributed to pore formation between the BGp layers. According to Song [17], the microstructure of biochar particularly pore size and distribution, is directly influenced by pyrolysis conditions. The BOGp surface exhibits reduced porosity, likely due to an increase in crystalline phases generated during the oxidation process.

3.2.2. Surface state

The BET analysis results are summarized in Table 4.

Table 4. BET parameters.

	Surface (m^2/g)	Pore Volume (cm^3/g)	Pore Diameter (Å)
BGp	228.1969	0.017608	18.929
BOGp	340.3151	0.02387	18.99

Unlike the result observed with the iodine number measurement, BOGp exhibits a higher specific surface area than BGp, indicating a more developed internal surface area for BOGp. This observed difference could be explained by BGp's strong microporosity, which is inaccessible to N_2, or by specific chemical interactions with iodine. These results are consistent with those reported by Zhihao et al. [18], who observed specific surface area values ranging from 140 m^2/g to 432 m^2/g for graphene-like materials. Both adsorbents have relatively similar pore diameters (< 2 nm), indicating that they are primarily microporous [19]. These values suggest that BGp and BOGp mainly possess micropores, i.e., pores with a diameter smaller than 20 Å (2 nm). This characteristic implies that opposing pore walls could exert attractive forces on adsorbates and significantly enhance adsorption capacity [15,20], especially for zinc, which has an ionic diameter of < 2 nm. Ultimately, BGp and BOGp are microporous, although oxidative treatment had a significant impact on their pore structure. Although BOGp shows a reduction in certain pore volumes, its overall pore volume is greater than that of BGp [21]. The examination of surface functional groups by Fourier-transform infrared spectroscopy (FTIR) led to the FTIR spectra illustrated in Figure 3.

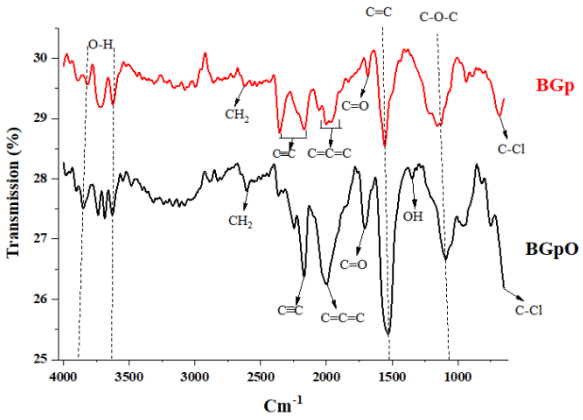

Figure 3. FTIR spectra of the adsorbents.

FTIR analysis reveals a band at 684.13 cm^{-1}, corresponding to the C-Cl functional group in BGp, while for BOGp, a slight shift is observed at 754.04 cm^{-1}. The presence of this group is associated with the graphitization and activation steps involving $ZnCl_2$ and $FeCl_3$. Oxidative treatment led to the appearance or intensification of several characteristic peaks in the BOGp spectrum. An absorption peak is observed for the carbonyl group (C=O) at 1709.13 cm^{-1}, a peak at 939.18 cm^{-1} (associated with C-O stretching vibrations), and a peak at 1085.26 cm^{-1} (assigned to C–O–C elongation vibrations) [22]. The presence of a peak at 1345.61 cm^{-1} indicates hydroxyl groups (OH), likely due to residual water between layers [23]. A distinct peak at 1,526.41 cm^{-1} is observed for both samples, with a noticeable intensification in BOGp, attributed to the skeletal vibration of C=C bonds in the graphene structure [24]. The vibration peaks at 2864.3 cm^{-1} for BGp and 2863.3 cm^{-1} for BOGp correspond to symmetric and asymmetric stretching vibrations of CH_2 groups present in grapheme [25]. The presence of these oxygen-containing groups confirms the oxidation process undergone by graphite, while the detection of surface hydroxyl groups suggests a hydrophilic nature for BOGp.

3.2.3. TGA/DTG analysis

The results of thermogravimetric analysis (TGA) and differential thermogravimetry (DTG) are presented in Figure 4.

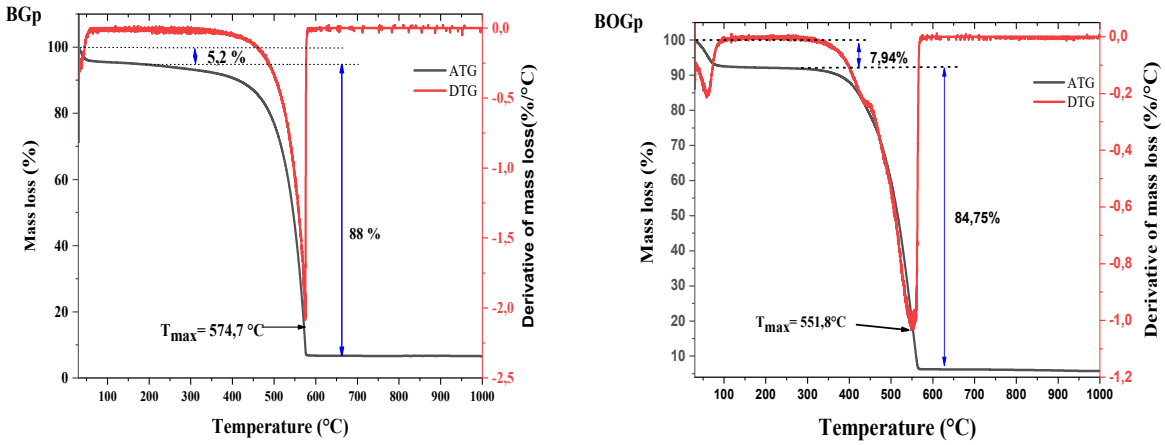

Figure 4. Thermogravimetric (TGA) and differential thermogravimetric (DTG) curves.

In the temperature range up to 200°C for BGp and 300°C for BOGp, a dehydration process occurs, resulting in a mass loss of 5.2% for BGp and 7.94% for BOGp. This dehydration phase is characterized by the release of

weakly bound water molecules and the degradation of some extractive compounds. The difference in mass loss between BGp and BOGp may be attributed to their distinct chemical compositions, which influence their dehydration behavior. Beyond this phase, a second stage extending up to 580°C for BGp and 565°C for BOGp led to mass reductions of 88% for BGp and 84.75% for BOGp. This phase corresponds to passive pyrolysis, necessary for converting organic residues into biochar. The DTG peak indicates the maximum degradation temperature (T_{max}) of residual polymers present in the adsorbents. BGp's residual polymers remain relatively more stable during the pyrolysis phase. This result suggests that oxidative treatment compromised the structural integrity of BOGp [26]. Furthermore, BGp may be more suitable for high-temperature applications. The residual mass after thermal treatment was 6.8% for BGp and 7.31% for BOGp, which could be associated with the presence of metal oxides.

3.3. Batch Adsorption

3.3.1. Mass effect

The results of zinc removal tests using different masses of BGp or BOGp are presented in Figure 5.

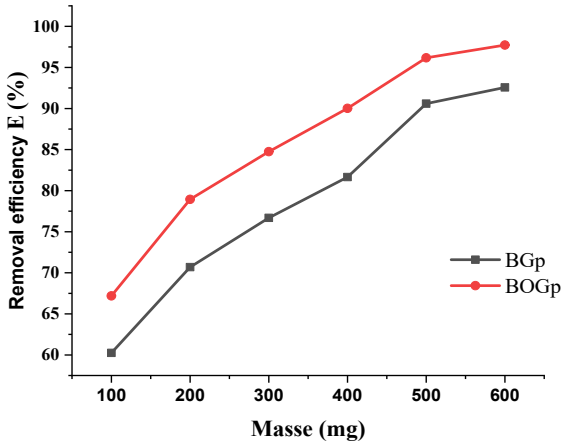

Figure 5. Elimination rate of zinc depending on the mass of BGp or BOGp.

The removal rate of Zn^{2+} per unit mass of adsorbent increases with the amount of adsorbent used, rising from 60.23% to 92.64% for BGp and from 67.20% to 97.85% for BOGp. This improvement in removal efficiency with increasing mass is attributed to the higher volume of active sites on the adsorbents, which enhances interaction with zinc ions. While this leads to more effective zinc adsorption, the process becomes less efficient despite the overall improvement in removal performance. A similar trend was reported in studies by Alhalili and Abdelrahman [27] . However, it should be noted that increasing the adsorbent mass may also promote aggregate formation. These aggregates could reduce the availability of binding sites, potentially compromising zinc removal efficiency [28]

3.3.2. Effect of contact time and adsorption kinetics

Figure 6 shows the zinc removal rate as a function of contact time. The graph indicates that the percentage of zinc removal increases with contact time, reaching equilibrium after 90 minutes for BGp and 105 minutes for BOGp.

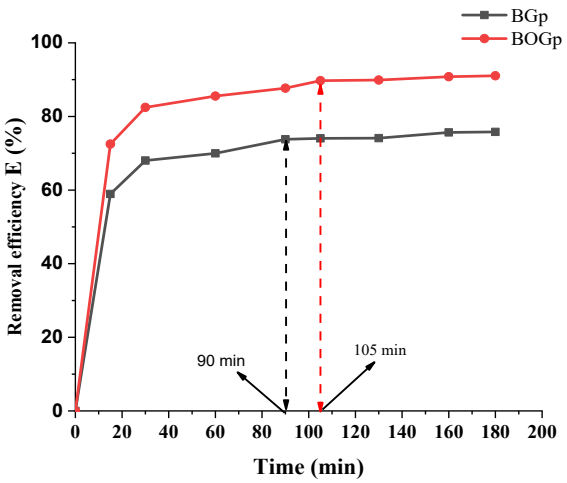

Figure 6. Zinc removal curves as a function of contact time.

At equilibrium, the zinc removal rate reaches 73.4% for BGp and 90.11% for BOGp. In the initial stage of the process, rapid adsorption is observed, primarily due to the high availability of active sites on the adsorbents' surface. These sites gradually become saturated until equilibrium is reached at 90 min for BGp and 105 min for BOGp. It is noted that the agitation duration, which determines the adsorbent-adsorbate contact time, influences the adsorption process. Sufficient contact time increases the driving force of the system, thereby reducing mass transfer resistance between the aqueous phase containing zinc and the adsorbents' surface. These varying contact times allow zinc ions to move more efficiently toward available adsorption sites, facilitating their removal. The reaction order, a key parameter for evaluating the adsorption mechanism, was determined using kinetic model theory. The different linear regression lines obtained from the kinetic models are presented in Figure 7.

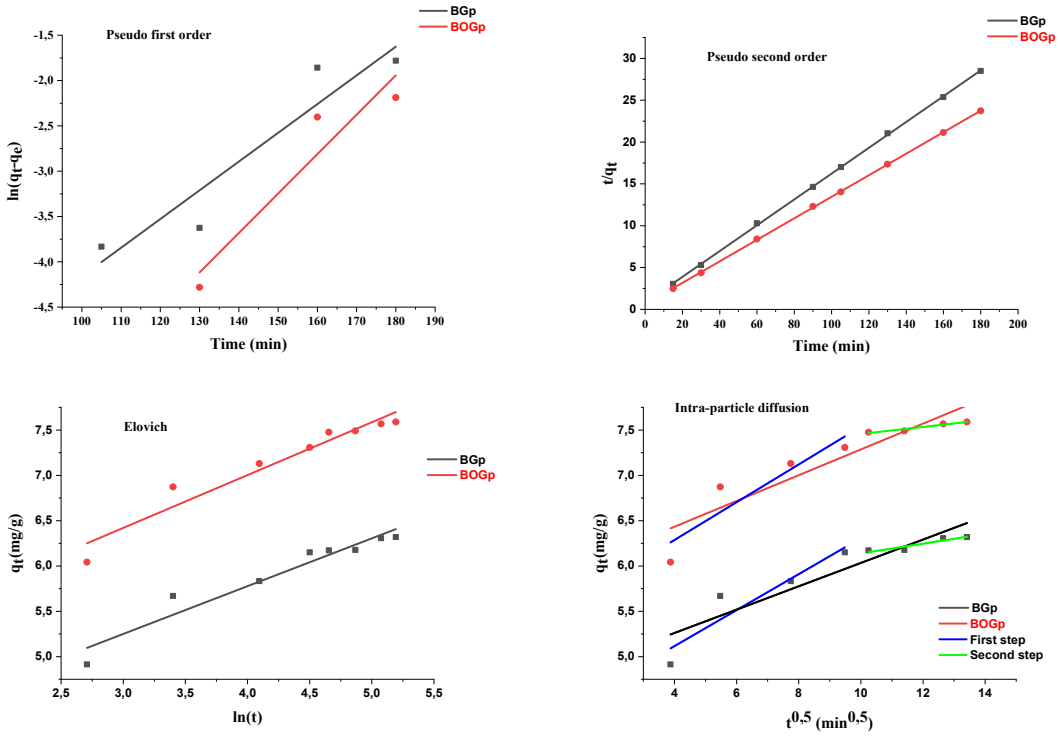

Figure 7. Linear regressions of kinetic models.

Kinetic parameters of the pseudo-first order, pseudo-second order, and Elovich models are summarized in Table 5

Table 5. Kinetic parameters of the pseudo first order, pseudo second order, and Elovich models

	Pseudo first order				Pseudo second order			Elovich		
	q_{exp}	k_1	q_e	R^2	k_2	$q_{théo}$	R^2	α	β	R^2
BGp	6.15	-0.07	0.0006	0.89485	0.03	6.48	0.9998	555.713	1.896	0.93
BOGp	7.48	-0.1	0.00005	0.90384	0.028	7.77	0.9999	1765.17	1.716	0.94

Analysis of Figure 7 reveals that for both adsorbents, the pseudo-second order model best describes the zinc adsorption process. Indeed, the theoretically calculated adsorption capacities closely match the experimental values, and the kinetic constants associated with the pseudo-second order model are more significant than those of the pseudo-first order model. Additionally, the coefficient of determination (R^2) for this model is close to 1 for both adsorbents. This indicates that zinc adsorption is not governed by a physisorption process, suggesting a minimal influence of van der Waals forces. Instead, chemical interactions likely play a dominant role. A strong correlation with the Elovich model further supports that chemisorption is a key mechanism in zinc adsorption on both adsorbents. The intraparticle diffusion model was used to assess the external diffusion step in the overall adsorption reaction. The linear regression of this model does not pass through the origin, implying that intraparticle diffusion alone does not control the reaction rate [29]. The kinetic parameters for this model are listed in Table 6.

Table 6. Parameters of intraparticle diffusion model

	Global step			First step			Second step		
	k_d	c	R^2	k_{d1}	c_1	R^2	k_{d2}	c_2	R^2
BGp	0.13	4.74	0.847	0.20	4.32	0.874	0.05	5.6	0.87
BOGp	0.14	5.86	0.846	0.21	5.45	0,847	0.04	7.07	0.94

The values of the overall diffusion rate constants (k_d) for BGp and BOGp indicate that the diffusion process is generally slow. The intraparticle diffusion process occurs in two distinct stages. The first stage, characterized by rapid diffusion, shows diffusion coefficients of k_{d1} = 0.2 mg/(g·min$^{0.5}$) for BGp and 0.21 mg/(g·min$^{0.5}$) for BOGp, suggesting diffusion through the adsorbents' macropores [30]. The second stage, which is slower, is represented by coefficients of k_{d2} = 0.04 mg/(g·min$^{0.5}$) for BGp and k_{d2} = 0.05 mg/(g·min$^{0.5}$) for BOGp. This phase is associated with micropore diffusion, which becomes the rate-limiting step in the overall diffusion process. These results demonstrate that the slow nature of intraparticle diffusion suggests this phenomenon cannot solely govern the overall adsorption reaction rate.

3.3.3. Concentration effect and adsorption isotherm

The influence of zinc concentration in the solution was studied and illustrated in Figure 8. A gradual increase in removal efficiency was observed with the rise in initial zinc concentration, reaching 96% for BGp and 98% for BOGp. This concentration effect is attributed to the increase in driving force resulting from the concentration gradient, which facilitates the passive transport of zinc ions toward the adsorbents' surface. Indeed, a high initial zinc concentration in the aqueous phase creates a greater concentration difference between the liquid phase and the solid phases of the adsorbents. This stronger driving force reduces the mass transfer resistance between the zinc-containing aqueous phase and the adsorbents' surface. As a result, it promotes the

movement of zinc from the liquid phase to the adsorption sites of the materials, enabling more efficient zinc removal until the saturation of the active sites of the given adsorbent is reached.

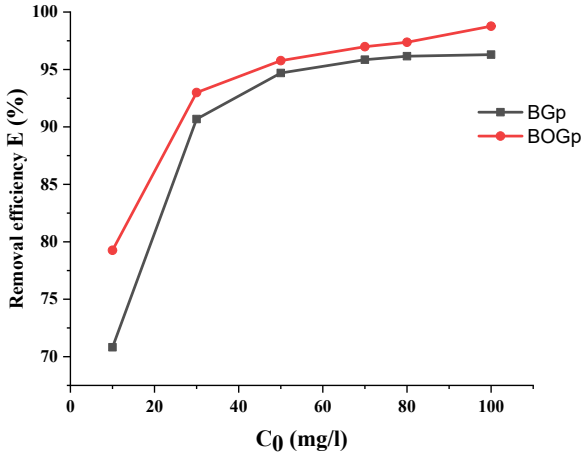

Figure 8. Zinc removal curves as a function of zinc concentration.

The Freundlich, Langmuir, and Temkin models were applied to understand the adsorption process behavior on the adsorbents. Figure 9 illustrates the linear regressions obtained from the isotherm model equations.

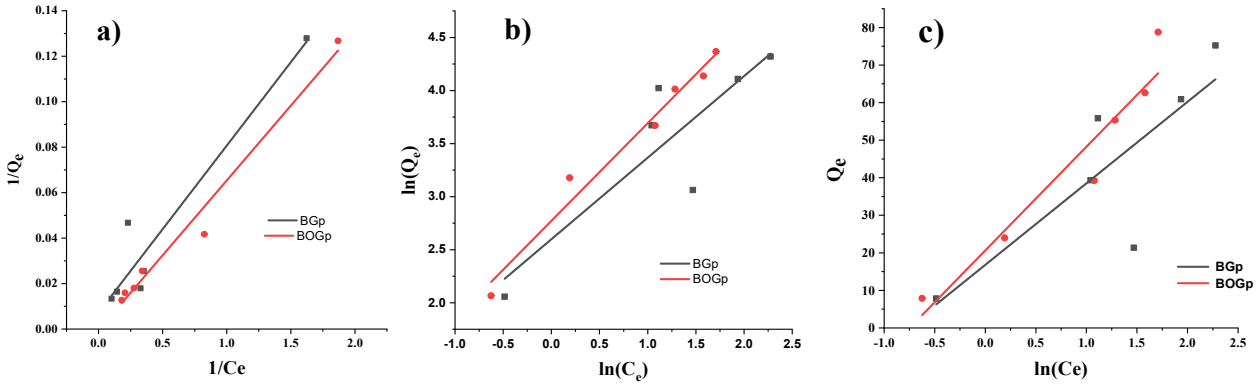

Figure 9. Linear regressions of the isotherm models: a) Langmuir; b) Freundlich; c) Temkin.

The model parameters calculated from the linear regressions of the Langmuir, Freundlich, and Temkin models are presented in Table 7.

Table 7. Parameters of the studied adsorption isotherm models

	Langmuir			Freundlich			Tempkin		
	q_{max}	R_L	R^2	n	K_F	R^2	K_T	b_T	R^2
BGp	138,12	0,5	0,79	2,6	2,156	0,92	3,64	1680,307	0,88
BOGp	158,98	0,51	0,87	2,8	3,51	0,98	5,81	2064,203	0,92

Figure 9-a shows that the experimental results do not follow the Langmuir model, indicating a non-homogeneous surface of the adsorbents and strong interactions between the adsorbed zinc layers. The R_L values for BGp and BOGp are 0.5 and 0.51, respectively, suggesting favorable zinc adsorption on both adsorbents. These closely matched values reflect similar adsorption efficiency behaviors. The determination coefficients

(R^2) for the Freundlich model (Table 7) remain higher than those of the other models, confirming its suitability for describing the zinc adsorption process by both adsorbents [31]. Furthermore, the heterogeneity factors (n > 1) indicate a favorable chemisorption process on a heterogeneous, multilayer surface. However, BGp exhibits slightly more pronounced heterogeneity, and a higher adsorption strength (K_F) compared to BOGp, which could positively influence BOGp's adsorption capacity under real conditions [31,32]. The Tempkin model analysis (Figure 9-c) corroborates the surface heterogeneity predicted by the Freundlich model, showing a good correlation with experimental data. The adsorption heats (b_T = 1680.307 J/mol for BGp and b_T = 2064.203 J/mol for BOGp) confirm that zinc chemisorption by both adsorbents is exothermic. However, interactions between zinc ions and the adsorbents may lead to a linear decrease in adsorption heat with surface coverage. BOGp demonstrates a stronger affinity (KT) for zinc than BGp, likely due to more favorable chemical interactions resulting from oxidative treatment [33].

4. Conclusion

Palm kernel shells, often regarded as waste, were successfully converted into graphene-like biochar (BGp) through graphitization-activation processes, followed by oxidation (BOGp). X-ray diffraction (XRD) analysis revealed significant modifications in the crystalline structure, while FTIR spectroscopy highlighted alcohol and carboxyl functional groups, confirming the oxidation of BOGp. Both materials exhibit low moisture content, moderate density, and pHpzc values of 4 (BOGp) and 7.3 (BGp). Zinc removal tests in aqueous solutions demonstrated effective elimination by both adsorbents, with the adsorption process following pseudo-second-order kinetics. Isotherm analysis confirmed an exothermic chemisorption process best described by the Freundlich and Tempkin models. These findings highlight the potential to efficiently convert biomass waste into effective materials for zinc removal and potentially other hazardous trace metals from contaminated water.

References

[1] Oladimeji, T. E., Oyedemi, M., Emetere, M. E., Agboola, O., Adeoye, J. B., & Odunlami, O. A. (2024). Review on the impact of heavy metals from industrial wastewater effluent and removal technologies. *Heliyon, 10*(22), Article e40370. https://doi.org/10.1016/j.heliyon.2024.e40370

[2] Mohammadpour, A., Gharehchahi, E., Gharaghani, M. A., Shahsavani, E., Golaki, M., Berndtsson, R., & Khosravi, H. (2024). Assessment of drinking water quality and identifying pollution sources in a chromite mining region. *Journal of Hazardous Materials, 480*, Article 136050. https://doi.org/10.1016/j.jhazmat.2024.136050

[3] Sumaya, M. U., Maria, K. H., Toma, F. T. Z., Zubair, M. A., & Chowdhury, M. T. (2023). Effect of stabilizer content in different solvents on the synthesis of ZnO nanoparticles using the chemical precipitation method. *Heliyon, 9*(10), Article e20871. https://doi.org/10.1016/j.heliyon.2023.e20871

[4] Raj, R., Mayank, M., & Laiju, A. R. (2024). Removal of zinc metal by ion exchanger technique using Amberlite IRA-120. *IOP Conference Series: Earth and Environmental Science, 1326*, Article 012135. https://doi.org/10.1088/1755-1315/1326/1/012135

[5] Sosa, S. M., Huertas, R., & Pereira, V. J. (2023). Combination of zinc oxide photocatalysis with membrane filtration for surface water disinfection. *Membranes, 13*(1), Article 56. https://doi.org/10.3390/membranes13010056

[6] Xu, C., Zhou, J., Yin, S., Wang, Y., Zhang, L., Hu, S., & Li, J. (2021). Solvent extraction and separation of zinc-iron from spent pickling solution with tri-n-octylamine. *Separation and Purification Technology, 278*, Article 119579. https://doi.org/10.1016/j.seppur.2021.119579

[7] Cherono, F., Mburu, N., & Kakoi, B. (2021). Adsorption of lead, copper and zinc in a multi-metal aqueous solution by waste rubber tires for the design of single batch adsorber. *Heliyon, 7*(10), Article e08254. https://doi.org/10.1016/j.heliyon.2021.e08254

[8] Trivedi, Y., Sharma, M., Mishra, R. K., Sharma, A., Joshi, J., Gupta, A. B., & Kumar, A. (2025). Biochar potential for pollutant removal during wastewater treatment: A comprehensive review of separation mechanisms, technological integration, and process analysis. *Desalination, 600*, Article 118509. https://doi.org/10.1016/j.desal.2024.118509

[9] Xiao, X., Chen, B., Zhu, L., & Schnoor, J. L. (2017). Sugar cane-converted graphene-like material for the superhigh adsorption of organic pollutants from water via coassembly mechanisms. *Environmental Science & Technology, 51*(21), 12644–12652. https://doi.org/10.1021/acs.est.7b03639

[10] Panicker, N. J., Das, J., & Sahu, P. P. (2020). Synthesis of highly oxidized graphene (HOG) by using HNO3 and KMnO4 as oxidizing agents. *Materials Today: Proceedings*. Advance online publication. https://doi.org/10.1016/j.matpr.2020.05.037

[11] Yannick, D. D., Zoungranan, Y., Dobi-Brice, K. K., Lynda, E., & Tchirioua, E. (2023). Graphene-like biochar from agricultural waste for cyanide removal: Kinetic study and adsorption isotherms. Science *Journal of Chemistry, 11*(5), 167–176. https://doi.org/10.11648/j.sjc.20231105.12

[12] Yannick, D. D., Zoungranan, Y., Dobi-Brice, K. K., Lynda, E., & Tchirioua, E. (2024). Cyanide removal by graphene-type oxidized biochar: Kinetic study and adsorption isotherms. *World Journal of Advanced Research and Reviews, 22*(1), 660–670. https://doi.org/10.30574/wjarr.2024.22.1.1075

[13] Lopez-Ramon, M. V., Stoeckli, F., Moreno-Castilla, C., & Carrasco-Marin, F. (1999). On the characterization of acidic and basic surface sites on carbons by various techniques. *Carbon, 37*(8), 1215–1221. https://doi.org/10.1016/S0008-6223(98)00317-0

[14] Anderson, N., Gu, H., & Bergman, R. (2021). Comparison of novel biochars and steam activated carbon from mixed conifer mill residues. *Energies, 14*(24), Article 8472. https://doi.org/10.3390/en14248472

[15] Chang, B., Guo, Y., Li, Y., Yin, H., Zhang, S., Yang, B., & Dong, X. (2015). Graphitized hierarchical porous carbon nanospheres: Simultaneous activation/graphitization and superior supercapacitance performance. *Journal of Materials Chemistry A, 3*(18), 9565–9577. https://doi.org/10.1039/C5TA00867K

[16] Asano, N., Lu, J., Asahina, S., & Takami, S. (2021). Direct observation techniques using scanning electron microscope for hydrothermally synthesized nanocrystals and nanoclusters. *Nanomaterials, 11*(4), Article 908. https://doi.org/10.3390/nano11040908

[17] Song, N.-J., Guo, N., Ma, C., Zhao, Y., Li, W., & Li, B. (2023). Modulating the graphitic domains and pore structure of corncob-derived hard carbons by pyrolysis to improve sodium storage. *Molecules, 28*(8), Article 3595. https://doi.org/10.3390/molecules28083595

[18] Zhang, Z., Schniepp, H. C., & Adamson, D. H. (2019). Characterization of graphene oxide: Variations in reported approaches. *Carbon, 154*, 510–521. https://doi.org/10.1016/j.carbon.2019.07.103

[19] Huang, M., Chou, C., & Teng, H. (2002). Pore-size effects on activated-carbon capacities for volatile organic compound adsorption. *AIChE Journal, 48*(8), 1804–1810. https://doi.org/10.1002/aic.690480820

[20] Sierra, U., Álvarez, P., Blanco, C., Granda, M., Santamaría, R., & Menéndez, R. (2016). Cokes of different origin as precursors of graphene oxide. *Fuel, 166*, 400–403. https://doi.org/10.1016/j.fuel.2015.10.112

[21] Yu, Z., Wang, W., Gao, H., & Liang, D. (2020). Properties analysis and preparation of biochar–graphene composites under a one-step dip coating method in water treatment. *Applied Sciences, 10*(11), Article 3689. https://doi.org/10.3390/app10113689

[22] Krishnamoorthy, K., Veerapandian, M., Yun, K., & Kim, S.-J. (2013). The chemical and structural analysis of graphene oxide with different degrees of oxidation. *Carbon, 53*, 38–49. https://doi.org/10.1016/j.carbon.2012.10.013

[23] Alam, S. N., Sharma, N., & Kumar, L. (2017). Synthesis of graphene oxide (GO) by modified Hummers method and its thermal reduction to obtain reduced graphene oxide (rGO). *Graphene, 6*(1), 1–18. https://doi.org/10.4236/graphene.2017.61001

[24] Song, C., Wu, D., Zhang, F., Liu, P., Lu, Q., & Feng, X. (2012). Gemini surfactant assisted synthesis of two-dimensional metal nanoparticles/graphene composites. *Chemical Communications, 48*(16), 2119–2121. https://doi.org/10.1039/c2cc16890a

[25] Spitalsky, Z., Danko, M., & Mosnacek, J. (2011). Preparation of functionalized graphene sheets. *Current Organic Chemistry, 15*(8), 1133–1150. https://doi.org/10.2174/138527211795202988

[26] Uddin Monir, M., Muntasir Shovon, S., Ahamed Akash, F., Habib, M. A., Techato, K., Abd Aziz, A., & Chowdhury, A. A. (2024). Comprehensive characterization and kinetic analysis of coconut shell thermal degradation: Energy potential evaluated via the Coats-Redfern method. *Case Studies in Thermal Engineering, 55*, Article 104186. https://doi.org/10.1016/j.csite.2024.104186

[27] Alhalili, Z., & Abdelrahman, E. A. (2024). Efficient removal of Zn(II) ions from aqueous media using a facilely synthesized nanocomposite based on chitosan Schiff base. *Scientific Reports, 14*, Article 17598. https://doi.org/10.1038/s41598-024-68745-5

[28] Fouda-Mbanga, B. G., Onotu, O., & Tywabi-Ngeva, Z. (2024). Advantages of the reuse of spent adsorbents and potential applications in environmental remediation: A review. *Green Analytical Chemistry, 11*, Article 100156. https://doi.org/10.1016/j.greeac.2024.100156

[29] Silva, L. M. S., Muñoz-Peña, M. J., Domínguez-Vargas, J. R., González, T., & Cuerda-Correa, E. M. (2021). Kinetic and equilibrium adsorption parameters estimation based on a heterogeneous intraparticle diffusion model. *Surfaces and Interfaces, 22*, Article 100791. https://doi.org/10.1016/j.surfin.2020.100791

[30] Wang, J., & Guo, X. (2022). Rethinking of the intraparticle diffusion adsorption kinetics model: Interpretation, solving methods and applications. *Chemosphere, 309*(Pt 2), Article 136732. https://doi.org/10.1016/j.chemosphere.2022.136732

[31] Bonilla-Petriciolet, A., Mendoza-Castillo, D. I., Dotto, G. L., & Duran-Valle, C. J. (2019). Adsorption in water treatment. In *Reference module in chemistry, molecular sciences and chemical engineering*. Elsevier. https://doi.org/10.1016/B978-0-12-409547-2.14390-2

[32] Zhu, Y., Yi, B., Yuan, Q., Wu, Y., Wang, M., & Yan, S. (2018). Removal of methylene blue from aqueous solution by cattle manure-derived low temperature biochar. *RSC Advances, 8*(36), 19917–19929. https://doi.org/10.1039/C8RA03018A

[33] Mekhalef Benhafsa, F., Kacha, S., Leboukh, A., & Belaid, K. D. (2018). Étude comparative de l'adsorption du colorant Victoria Bleu Basique à partir de solutions aqueuses sur du carton usagé et de la sciure de bois. *Revue des Sciences de l'Eau, 31*(2), 109–126. https://doi.org/10.7202/1051695ar